WATER RESOURCES RESEARCH, VOL. 49, 2473–2488, doi:10.1002/wrcr.20075, 2013

Transient groundwater dynamics in a coastal aquifer: The effects of tides, the lunar cycle, and the beach profile

Elena Abarca,[1] Hanan Karam,[1] Harold F. Hemond,[1] and Charles F. Harvey[1]

Received 10 July 2012; revised 16 December 2012; accepted 20 December 2012; published 22 May 2013.

[1] Detailed field measurements are combined with a numerical modeling to characterize the groundwater dynamics beneath the discharge zone at Waquoit Bay, Massachusetts. Groundwater salinity values revealed a saline circulation cell that overlaid the discharging freshwater and grew and disappeared with the lunar cycle. The cell was initiated by a greater bay water infiltration during the new moon when high tides overtopped the mean high-tide mark, flooding the flatter beach berm and inundating a larger area of the beach. The dynamics of this cell were further characterized by a tracer test and by constructing a density-dependent flow model constrained to salinity and head data. The numerical model captured the growing and diminishing behavior of the circulation cell and provided the estimates of freshwater and saline water fluxes and travel times. Furthermore, the model enabled quantification of the relationship between the characteristics of the observed tidal cycle (maximum, minimum, and mean tidal elevations) and the different components of the groundwater circulation (freshwater discharge, intertidal saline cycling, and deep saline cycling). We found that (1) recharge to the intertidal saline cell is largely controlled by the high-tide elevation; (2) freshwater discharge is positively correlated to the low-tide elevation, whereas deep saline discharge from below the discharging freshwater is negatively correlated to the low-tide elevation. So, when the low-tide elevation is relatively high, more freshwater discharges and less deep saltwater discharges. In contrast when low tides are very low, less freshwater discharges and more deep salt water discharges; (3) offshore inflow of saline water is largely insensitive to tides and the lunar cycle.

Citation: Abarca, E., H. Karam, H. F. Hemond, and C. F. Harvey (2013), Transient groundwater dynamics in a coastal aquifer: The effects of tides, the lunar cycle, and the beach profile, *Water Resour. Res.*, *49*, 2473–2488, doi:10.1002/wrcr.20075

1. Introduction

[2] Tides often control coastal groundwater dynamics, driving submarine groundwater discharge (SGD) and hence the flux of solutes that SGD delivers to the ocean. Solutes that are important in the coastal environment include nitrate, a cause of coastal eutrophication; iron, soluble in its reduced state but a key solid-phase sorbent when oxidized; agricultural pesticides; and pharmaceutical residues from wastewater. Here we combine the detailed field measurements with a numerical model to characterize how the dynamics of the coastal groundwater system vary with the lunar cycle of tides resulting in changes in the SGD-mediated fluxes.

[3] Fresh groundwater discharge (FGD) to the sea is often bounded by two saline recirculation zones (Figure 1): below, by the deep saltwater wedge (DSW), which is the focus of traditional studies of seawater intrusion into coastal aquifers, and above, by a tidally driven recirculation cell called here the intertidal saltwater cell (ISC). The DSW exists because of the stable density stratification, with denser saltwater encroaching below the discharging freshwater [*Kohout*, 1964; *Cooper*, 1964], and is present in all coastal aquifers, confined or unconfined. At the interface between the freshwater and the DSW, mixing caused by diffusion and dispersion creates a convective region in which saline water that flows landward mixes into the freshwater and is subsequently flushed back to the ocean by the discharging flow. There are thus two fluxes associated with the DSW, the deep saltwater infiltration (DSI) of the ocean water and the deep saltwater discharge (DSD; Figure 1). At steady state, DSI equals DSD, and their value depends largely on the transverse dispersion [*Smith*, 2004; *Abarca et al*., 2007]. Additionally, tidal oscillations may enhance these fluxes [*Li et al*., 1999; *Destouni and Prieto*, 2003; *Prieto and Destouni*, 2005] by enhancing mixing.

[4] The ISC, by contrast, forms in unconfined aquifers beneath the intertidal zone but above discharging freshwater and has been the subject of field studies [*Lebbe*, 1999; *Urish and McKenna*, 2004; *Robinson et al*., 2006; *Henderson et al*., 2010]. The ISC is filled by the intertidal seawater infiltration (ISI) during high tides. Saltwater discharges back to the ocean at receding tides, comprising the

Additional supporting information may be found in the online version of this article.

[1]Department of Civil and Environmental Engineering, Massachusetts Institute of Technology (MIT), Cambridge, Massachusetts, USA.

Corresponding author: C. F. Harvey, Parsons Laboratory, Department of Civil and Environmental Engineering, Massachusetts Institute of Technology, 77 Massachusetts Ave., Room 48-309 Cambridge, MA 02139-4307, USA. (charvey@mit.edu)

©2013. American Geophysical Union. All Rights Reserved.
0043-1397/13/10.1002/wrcr.20075

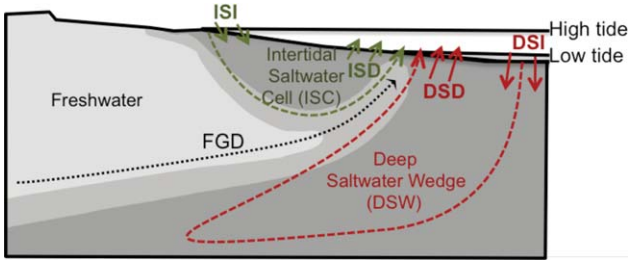

Figure 1. Groundwater regions and flow components in an unconfined coastal aquifer.

intertidal saltwater discharge (ISD). The dynamics of this tidally driven recirculating saltwater have been numerically simulated by *Lebbe* [1999], *Vandenbohede and Lebbe* [2006], and *Robinson et al*. [2006]. *Robinson et al*. [2006] describes a pseudo-steady-state ISC whose dimensions depend on the tidal amplitude, the magnitude of fresh groundwater flow toward the ocean [*Robinson et al*., 2007b], and the beach slope. *Robinson et al*. [2007a] found that spring and neap tides with different amplitudes result in changes in the dimensions of the ISC. Similar intertidal dynamics have been described in the tidally influenced saltwater marshes and rivers [*Wilson and Gardner*, 2006; *Westbrook et al*., 2005].

[5] The three discharging fluxes described above (FGD, ISD, and DSD) are the intrinsic components of the SGD. Characterizing the timing and location of discharge from these different components of the coastal groundwater system is important because they typically carry different solute loads to the sea. The FGD is typically most important for nitrate and for other contaminants originating on the upland watershed. The DSD is important for transport of nutrients mineralized in bottom sediments, and the ISD can transport metabolites of the shallow coastal aquifer [*Brovelli et al*., 2007; *Maji and Smith*, 2009; *Robinson et al*., 2009]. Furthermore, each of these fluxes carries different concentrations of environmental tracers, such as radium isotopes, that are measured in the coastal waters to quantify the groundwater discharge. At the field site in Waquoit Bay, *Michael et al*. [2011] found that FGD, ISD, and DSD had distinctly different compositions of radium isotopes, a finding that indicates that the dynamics of the groundwater system may be one of the factors affecting the isotopic composition of the coastal waters.

[6] Although tidal variability affects the ISC size and development [*Robinson et al*., 2007a], prior studies have assumed that it is a constant feature of the coastal aquifer. Our observations at Waquoit Bay, Massachusetts, however, reveal a system in which the ISC is not a permanent feature at the coastal aquifer; instead it can appear and disappear with the lunar cycle, with major effects on flow. In this work we aim at understanding how variability in the tides affects the ISC behavior, mixing patterns, and the temporal evolution of groundwater fluxes to the ocean. To this end, a comprehensive set of field measurements was carried out and interpreted with a numerical model of the tidally driven freshwater and saltwater flow that explains the observed transience of the ISC, elucidating how the periodicity of the ISC results from the lunar variations in the high-tide elevation and the beach profile. With the numerical model, we analyze (1) the transport of a solute moving through the ISC and (2) the temporal dynamics of the freshwater and saltwater fluxes (from the intertidal and the saltwater wedge) and (3) the dependence of these dynamics on the variations in the minimum, maximum, and mean tide elevations. The combination of the detailed observation and modeling enables us to track how SGDs from all the components of the groundwater system are affected by the tides.

2. Materials and Methods

2.1. Field Site

[7] Waquoit Bay is a nearly enclosed embayment located in the southwest coast of Cape Cod, Massachusetts (Figure 1). This bay, as other areas of Cape Cod, suffers from eutrophication linked to the anthropogenic nitrogen discharge through the groundwater to the bay [*Valiela et al*., 1990, 1992; *Bowen et al*., 2007]. The bay has been the subject of previous research on the SGD [*Cambareri and Eichner*, 1998; *Michael et al*., 2005; *Mulligan and Charette*, 2006] and of geochemical reactions in the subterranean estuary [*Charette and Sholkovitz*, 2006; *Spiteri et al*., 2008].

[8] Waquoit Bay is located along the southern margin of the groundwater mound called Sagamore Lens [*Janik*, 1987] and has an area of 3 km^2 and an average depth of 1 m [*Cambareri and Eichner*, 1998]. It is incised into the outwash plain deposited by the retreating Cape Cod Bay glacial lobe [*Oldale and Dillon*, 1981]. The unconfined aquifer consists of 100 to 120 m thick deposits of gravel, sand, and silt underlain by the less permeable deposits of till and bedrock below [*LeBlanc et al*., 1986]. The study site is located within the bluff area at the Head of the Bay (Figure 2), which is characterized by the outwash of a prograding glacial delta comprising a 11.3 m thick high-permeability aquifer overlying a low-permeability aquifer of 33.5 m thick. *Cambareri and Eichner* [1998] delineated the groundwater recharge areas based on the groundwater divides of the piezometric surface. According to their data, the area of recharge of the Head of the Bay is about 76 ha, with a recharge of 0.48–0.56 m/yr. A hydraulic gradient of 0.002 toward the ocean was calculated from their piezometric contours. *Mulligan and Charette* [2006] found that the hydraulic gradient at the Head of the Bay is not uniform. They estimated higher values of the gradient both under the bluff (0.015–0.022 at high and low tides, respectively) and in a flatter valley area (0.002–0.004). These gradients were estimated based on the measurements of heads in the wells located very near the coast, which are subject to high variability due to tides.

[9] *Michael et al*. [2005] observed the presence of the ISC at the Head of the Bay (valley area) but did not consider the possible transience of the ISC. *Henderson et al*. [2010] also found a salinity pattern consistent with the existence of the ISC by inverting electrical resistivity measurements along the same cross section described here.

2.2. Data Collection

[10] From 30 June to 26 August 2009, tidal fluctuations, groundwater heads, and salinity were measured regularly. Automatic level loggers (Solinst) were installed in four

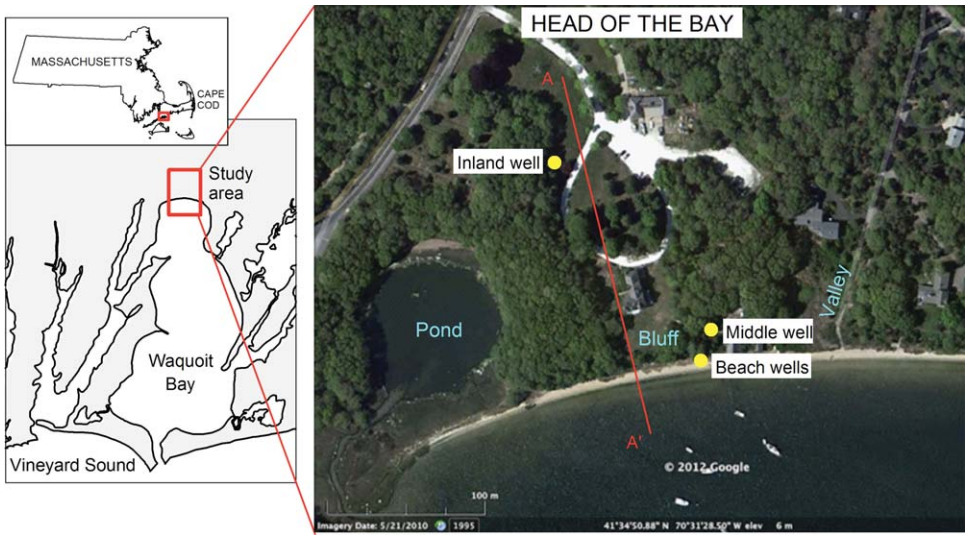

Figure 2. Field site location and map view showing the location of AA′ section and the location of wells with head measurements.

wells owned by the Waquoit Bay National Estuarine Research Reserve. The location of these wells is indicated in a plan view (Figure 2 and also projected in a cross section perpendicular to the coast in Figure 3). Although the wells are not perfectly aligned in the cross section, we assumed groundwater flow to be perpendicular to the coast line along the bluff area. Two wells are located at the beach at different depths (Beach1 and Beach2); the furthest well is located 120 m away from the coast (inland well) and a fourth well is located 20 m from the coast (middle well).

[11] Multidepth sampling piezometers were installed at the intertidal zone in a cross section perpendicular to the coast for salinity and chemical sampling (A1–J2 in Figure 3b). They were constructed by bundling 1/8″ inside

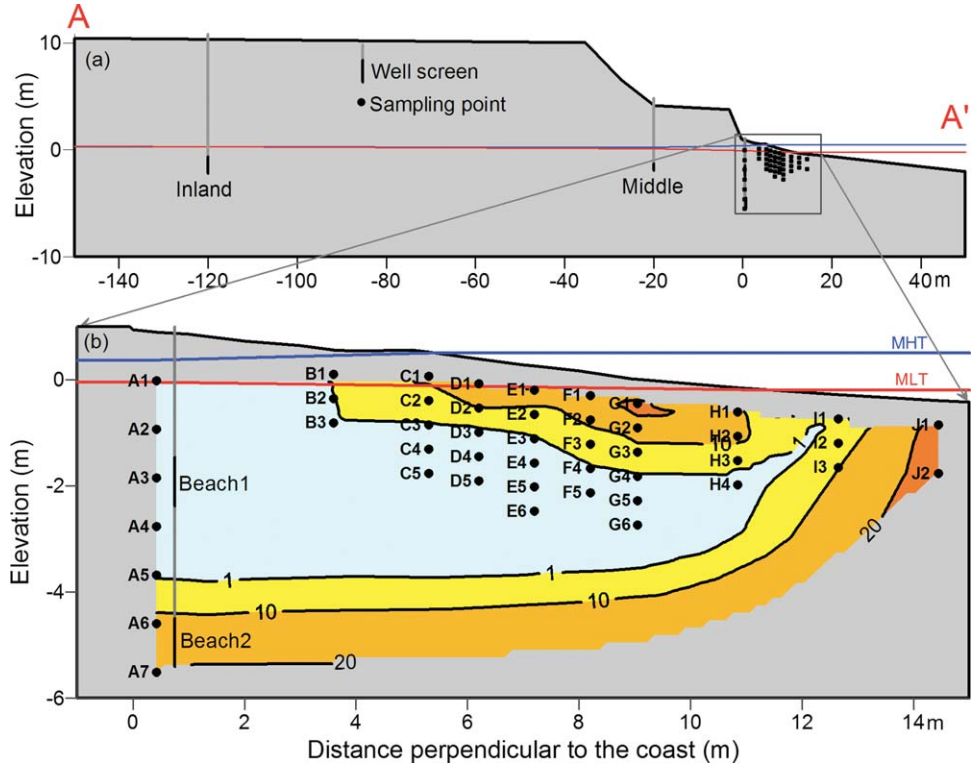

Figure 3. (a) Location of the measurement sites in a cross section AA′ and (b) location of the salinity sampling points at the intertidal zone and salinity contours before the tracer injection.

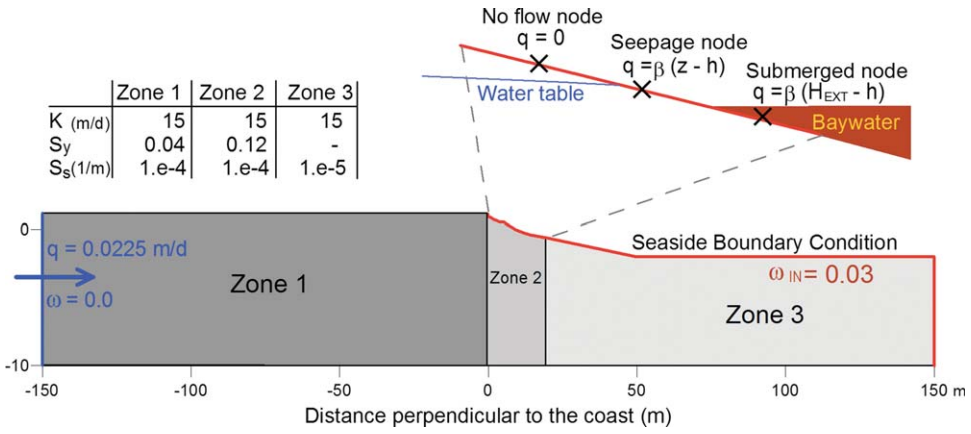

Figure 4. Dimensions and zonation of the numerical model.

diameter (ID) polyethylene tubes around a 3/8″ fiberglass rod. The bottom ends of the sampling tubes were covered with a screen. The bundles were installed by driving a 2″ ID galvanized steel pipe equipped with a disposable polyvinyl chloride knockout point. The casing was driven to the desired depth, the bundle piezometer was lowered down the pipe, the point was knocked out, and the pipe was withdrawn allowing sand to collapse around the bundle. In addition, a YSI 600XL sonde was installed below the low-water mark aligned with the bundle piezometers to track the local tidal fluctuations in the study area. All the pressure measurements were corrected for barometric changes when converted to hydraulic heads.

2.3. Tracer Injection

[12] We used a tracer injection to qualitatively characterize the groundwater velocity and travel times in the ISC. The tracer was injected during the high spring tide occurring at new moon (21 August 2009 at noon). Uranine (Na-fluorescein) was chosen as a tracer because it can be detected at very low concentrations; it is ecotoxicologically safe [*Behrens et al*., 2001]; its fluorescent intensity is not affected by the bay water salinity [*Smart and Laidlaw*, 1977; *Magal et al*., 2008]; and its adsorption is minimized in quartz sands at neutral pH [*Kasnavia et al*., 1999; *Flury and Wai*, 2003]. The background fluorescence of the groundwater was measured at all sampling points prior to the injection of the tracer. A previous salinity survey delineated the ISC (Figure 3a). Among the points with high salinity at the ISC, the most upstream one, D1, was selected as the injection point. Of Uranine (Na-fluorescein), 0.25g was added to 100 ml of water from D1, and this solution was injected into D1 with the help of a peristaltic pump. The injection took place immediately before the tide reached the location of the D bundle and therefore before a new infiltration event took place over D1. Pore water was sampled from the piezometers eight times during the first week after injection and six more times during the following month. Samples were collected in 9 ml test tubes, and fluorescence was immediately measured with a Turner Model 10 fluorometer.

2.4. Numerical Model

[13] Saturated-density-dependent groundwater flow and solute transport simulations were performed with the finite element code TRANSDENS [*Hidalgo et al*., 2005]. The upper aquifer (11 m) of Waquoit Bay was modeled in a 2-D vertical cross section perpendicular to the coast (Figure 4). The model domain (300 m long and 11 m thick) was discretized using an irregular triangular mesh with a higher resolution (0.4 m) in the intertidal zone. A sensitivity test to the grid size was performed to ensure that the solution was independent of the grid size.

[14] The domain was divided in three zones: the inland zone (zone 1), the intertidal zone (zone 2), and the submerged zone (zone 3). In zone 1 the water table is always within the model domain, remaining beneath the land surface. In zone 2, the water table moves below and above the top layer with the tides. When the beach face is submerged the water table is above the top model layer, but when the beach is exposed the water table may drop into the top layer. Zone 3 is always submerged below the sea. We simulated the movement of the water table in zones 1 and 2 by adjusting the saturated thickness of the top layer. When the water table shifts within a layer, the transmissivity (conductivity multiplied by saturated thickness) is adjusted. In the top layer, the storage coefficient is the specific yield S_y, and in the underlying layers that are fully saturated the storage coefficient is the specific storage S_s multiplied by the layer thickness. This approximation is a well-known modeling technique [*Neuman*, 1974; *Souza and Voss*, 1987; *Reilly and Harbaugh*, 1993; *Gingerich and Voss*, 2005; *Faunt et al*., 2011] that yields minimal loss of accuracy if drawdowns are relatively small compared to the saturated thickness of the unconfined aquifer.

[15] Changes in the tidal level above the offshore always submerged region (zone 3) drive both the pore pressure and the matrix stress on the underlying aquifer. In this zone, storage is parameterized by S_s, but the value of S_s was reduced from that in zones 1 and 2 to represent only the water compressibility, not the matrix compressibility. Because the tidal load changes the total stress but the effective stress remains the nearly constant, the pore volume will also remain nearly constant [*Wang*, 2000]. *Reeves et al*. [2000] and *Gardner and Wilson* [2006] showed that in marsh field studies large errors in the magnitude and timing of the saltwater fluxes across the seafloor boundary occurred when the sediment compressibility is included in the groundwater flow equation. Using a typical storage

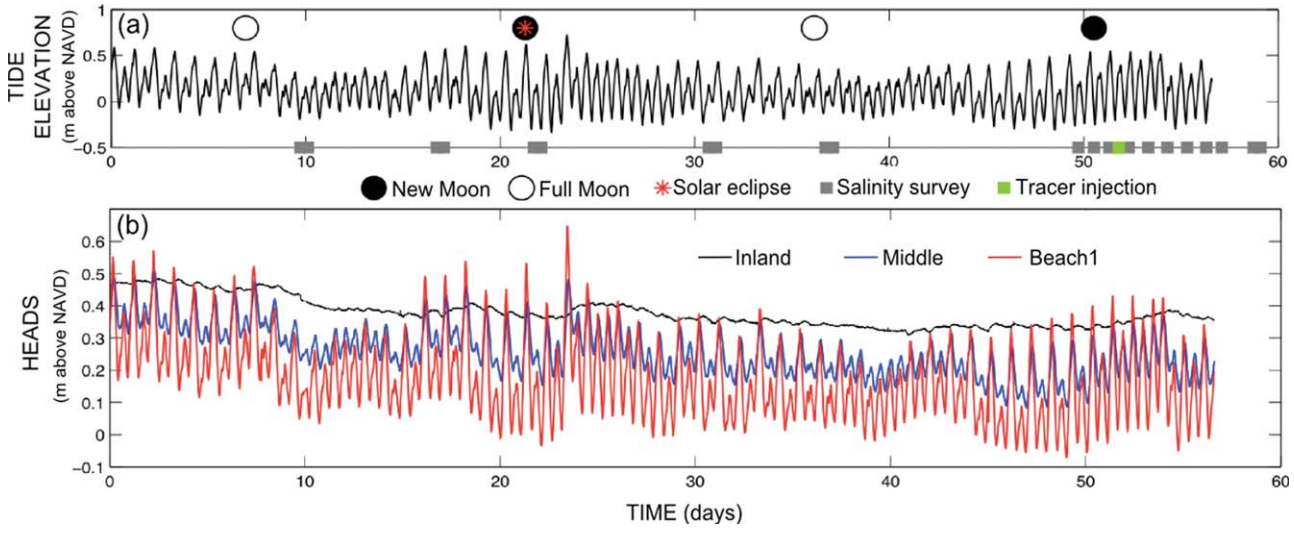

Figure 5. (a) Tide elevation at the studied site and timeline of the salinity and tracer surveys and (b) groundwater head measured at the inland, middle and Beach1 wells during two lunar cycles.

coefficient value of a confined sandy aquifer (1.0×10^{-3}), which would allow matrix compression in the submerged part of the aquifer, leads to an overestimation of the flows induced by the tidal pumping. Thus, we used a storage coefficient value of 1.0×10^{-5} that accounts for the water compressibility only.

2.4.1. Boundary Conditions

[16] The boundary conditions are (1) a constant freshwater inflow through the inland boundary ($q_f = 0.0225$ m/d) and (2) a nonlinear Cauchy boundary condition for the seaside boundary. In the intertidal zone, the parameters of the boundary condition vary with the tides [*Robinson et al*., 2006, 2007b]. Our model differs from that of *Robinson et al*. [2006] in the implementation of the seaward boundary condition that allows for seepage faces. The following nonlinear Cauchy boundary condition was implemented in the code and applied to the nodes that represent the beach surface in zone 2 (Figure 4). At a given time, the flow q_i [L^2/T] through node i is calculated as

$$q_i(h_i) = \beta_0 L_i (H_{\mathrm{EXT}} - h_i)\ H_{\mathrm{EXT}} > z, \tag{1}$$

$$q_i(h_i) = \beta_0 L_i (z - h_i)\ H_{\mathrm{EXT}} < z < h_i, \tag{2}$$

$$q_i(h_i) = 0\ h_i < z, \tag{3}$$

[17] where β_0 is the leakage coefficient; L_i is the length associated with node i; z is the node elevation; H_{EXT} is the prescribed external head, which corresponds to the measured tidal elevation presented in Figure 5a; and h_i is the calculated head at node i. Notice that the boundary condition depends on both the tidal elevation and the calculated head for every node of the boundary. Therefore, three cases may arise (Figure 4): (1) if the node is submerged there is connection between the sea and the aquifer (equation (1)); (2) if the node is emerged and the calculated head in the node is higher than its elevation, there is also a connection which allows drainage of the aquifer above the water line and the formation of a seepage face (equation (2)); and (3) if the node is emerged and the head at the node is lower than its elevation, the boundary becomes a no-flow boundary (equation (3)). The value of the leakage coefficient (β_0) represents the conductance of the seafloor sediment. A high value of the leakage coefficient describes a conductive interface between the ocean and the aquifer, whereas a small value represents a low-conductivity interface, for example, a muddy layer, and will result in a well-developed seepage face.

[18] The transport boundary conditions are zero salt mass flux across the bottom and inland boundaries. At the bay boundary (red line in Figure 4), a salt mass flux boundary condition was specified so that the fluid enters the aquifer with the bay water salt concentration but exits with the aquifers' salt concentration (for details, see, e.g., *Abarca et al*. [2007]).

2.4.2. Initial Conditions

[19] The coastal groundwater system is constantly shifting with tides and changes in the inland water table. Thus, determining an initial condition for a transient simulation is challenging. Here the initial conditions were also calibrated to fit the observed initial heads and location of the DSW. The initial conditions were the result of two consecutive simulations: first, a simulation without tidal forcing (with a sea level elevation of −0.25 m) was performed, and the freshwater inflow was modified until the interface matched the depth of the interface measured at the A wells (Figure 3). That simulation was used as a initial condition of a transient simulation with tides. The first two measured tidal cycles were repeated to create the tidal signal. The heads calculated in that simulation were compared with the initial heads measured at the inland, middle, and beach wells, and when a good match was achieved for the three wells at the same time step, that time step was used as a initial condition for the study period. Therefore, the model calibration was an iterative process carried out until both a good fit of the initial conditions and the evolution of heads and salinity during the simulation period was achieved.

2.4.3. Groundwater Age Simulation

[20] Simulations of groundwater age provide insight into the residence time of groundwater in the different regions of the coastal groundwater system. For example, it delineates the areas of the fast groundwater recirculation which can be useful to interpret the chemical patterns in the coastal aquifer. One approach that has been applied to simulate the groundwater residence times in the coastal aquifers is to calculate the travel times along the flow lines [*Robinson et al*., 2007b]. In this approach, the flow lines are calculated using a steady-state groundwater flow simulation with the phase-averaged periodic boundary conditions to reproduce tides. However, this approach simplifies the flow field and does not account for mixing of waters with different travel times. Here we use groundwater aging as a method to evaluate the residence time. This method implicitly includes mixing, an intrinsic transport mechanism in this tidally influenced system. In addition, diurnal variability in the tidal signal makes the phase-averaged method unsuitable for our case.

[21] The aging of groundwater in the system was calculated taking advantage of the equivalence between the groundwater age transport equation and the solute transport equation [*Goode*, 1996; *Varni and Carrera*, 1998; *Bethke and Johnson*, 2008].

$$\frac{\partial(\theta\tau)}{\partial t} = \nabla(\mathbf{D}\nabla\tau) - \nabla(q\tau) + q_r\tau' + A\theta, \tag{4}$$

where θ is the volumetric water content, τ [M/L^3] is the groundwater age, t is the time, $\mathbf{D}$ is the dispersion tensor, q [M/L] is Darcy's flow, q_r is the water flux entering the domain through the boundary conditions, τ' is the age of the water sources, and A is the aging rate (equivalent to a zero-order production rate [M/L^3/T]) which is equal to 1.

[22] An age mass flux is prescribed in all the flow boundary conditions. The age of all incoming groundwater through the boundaries, τ', is set to 0. Therefore, the calculated freshwater age is relative to the time when it traverses the inland boundary. In the case of the saline groundwater, the aging calculated by the model reflects its complete travel time through the system. Therefore, this simulation allows us to identify the areas of the fast saltwater recirculation on the basis of the low calculated ages.

[23] The age simulation follows the same sequence of simulations as the solute transport model: a steady-state age transport in a system with no tides is followed by a transient simulation with a synthetic tide signal that finally leads to the simulation with the tidal signal measured during the study period.

3. Results

[24] Groundwater heads and the tidal elevation were monitored every 10 min for a period of 56 days starting on 30 June 2009 at 1630 h local time (time origin in the following figures). This monitoring period includes two lunar cycles with four spring and neap cycles (two full moon and two new moon events; Figure 5a). The tidal amplitude reaches its maximum (0.9 m) around new moon, while the spring tides occurring around full moon (0.6 m) are not much higher than the neap tides (0.4 m). On 22 July, the sun, moon, and earth aligned (a solar eclipse!), and 2 days later the maximum high tide of the studied period occurred.

3.1. Groundwater Heads

[25] Figure 5b demonstrates how the amplitude of the tidally driven groundwater head oscillations decreases with the distance from the beach for heads measured in the three observation wells. Heads measured at Beach2 were nearly the same as at Beach1, so only Beach1 was plotted. Head response to tidal fluctuations is nonlinear, with the response to extreme high tides magnified. At very high tides, around new moon, the groundwater gradient reverses completely, heads being higher next to the coast (Beach1) than in the middle and inland wells. When this happens, even the inland well, located around 120 m from the intertidal zone, shows only a response of 1 cm to high tides.

3.2. Salinity Data

[26] Salinity was characterized from the pore water samples extracted from the piezometers. The sampling grid is shown in Figure 3, and the sampling days are marked with gray rectangles in Figure 5a. Electrical conductivity measurements of the pore water were converted to practical salinity following the UNESCO 1983 polynomial [*UNESCO*, 1983]. The measured salinity (contours in Figure 6) indicates a very dynamic ISC. ISC was consistently small or did not exist around the neap tides preceding new moon and grew to its maximum extent during the high spring tides of the new moon. The ISC, when fully developed, reaches more than 2 m deep and extends horizontally between points B1 and H1. The DSW is poorly constrained by data, only points A5–A7 and J1–J2 (Figure 3b) persistently delimit the location of the DSW-freshwater interface. The values at points I3, H4, and G6 show a vertical movement of the DSW that correlates well with the growing and vanishing cycle of the ISC. When the ISC develops, the weight of the saline water and the shift in groundwater pathways caused by extreme low tides and deeper freshwater pathways push the DSW down (wells H4 and G6 get fresher) and seaward (I3 and J1 get fresher). The freshwater discharge region is constrained between the bundles H and I (Figure 3a).

3.3. Tracer Injection

[27] The measured tracer concentrations indicate that the tracer plume moves slowly, following the saltwater flow along the ISC (Figure 6). The tracer moves downward, driven by the buoyancy effects and the new infiltration events after injection. The horizontal movement of the tracer is mainly seaward toward the lower part of the ISC where it discharges to the ocean. A small landward movement of the center of mass of the tracer plume, when sampled both during high and low tides, evidenced horizontal oscillations of the tracer driven by tides. However, seaward movement is dominant. Most of the tracer disappeared together with the ISC, 2 weeks after the injection. Later, the ISC grew again and the relict tracer remaining from the previous cycle was displaced downward by the newly infiltrated saltwater.

[28] The results indicate that flow in the ISC is dominated by bay water infiltration during the new moon, after which it is characterized by slow advection and dilution until discharging to the bay. While there appears to be

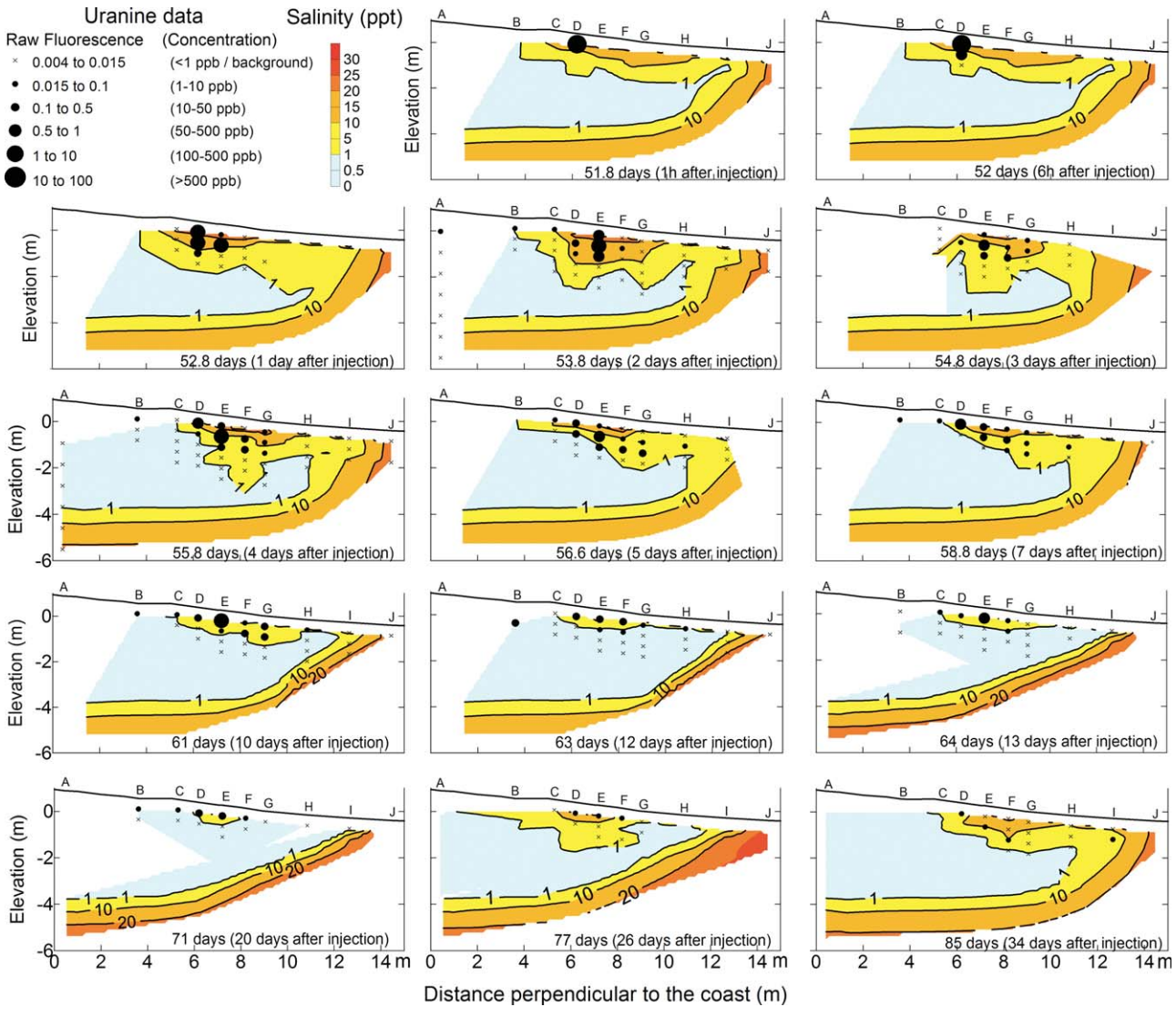

Figure 6. Salinity contours based on the measured Electrical Conductivity (EC) showing a complete ISC cycle and tracer test evolution during 1 month after injection. The middle part of the DSW interface has been interpolated between the bundles A in one extreme and J, I (and H4 and G6 when the interface moves up) in the other.

continuous flow through the ISC, the shifting imbalance between the saline inflow and outflow means that the ISC grows and shrinks. In fact, the center of mass of the tracer plume moves less than 2 m. Most of the tracer is diluted by mixing with freshwater and is then flushed out slowly in low concentrations. This slow flow suggests that low values of the hydraulic conductivity occur in the intertidal zone. The residence time of the injected tracer is around 2 weeks, a much longer time than the residence time (40–80 h) of a bromide tracer injected in the ISC (valley area) on 27 August 2001 [*Michael*, 2004]. That injection took place right at the third lunar quarter (neap tides), when the ISC was likely to be declining. The discrepancy in residence times acknowledges the control of the ISC cycle in the transport of solutes in the intertidal zone. Longer residence times are expected for bay water infiltrated when the ISC is growing, as in our tracer test.

3.4. Model Calculations

[29] We used the field data to develop a numerical model of the flow and salt-transport system and then used this model to calculate fluxes over the duration of the data collection. In this way, the model enabled us to extrapolate our measured heads, salinity, and prior hydraulic data to estimate fluxes. This is accomplished by first adjusting the unknown parameters in the model to fit all the data, then using the calibrated model to calculate the saline and freshwater fluxes.

[30] The calibration was done manually until a model was found that had a minimum number of parameter zones and reasonable parameter values that capture the key features of the system. These key features are (1) the growing and waning cycle of the ISC, (2) the maximum ISC extension, (3) the ISC mixing zone defined by the salinity gradient observed between points E1–E3 (see location in Figure

Table 1. Parameters Used in the Simulations

Parameter	Value	
φ	0.30	Porosity
K	15 m/d	Hydraulic permeability (isotropic)
α_L	0.1 m	Longitudinal dispersivity
α_T	0.01 m	Transverse dispersivity
D_m	1.0 E-5 m^2/d	Molecular diffusion coefficient
q_f	0.0225 m/d	Freshwater recharge rate
β_0	1000 m/d	Seaside boundary leakage coefficient
ω_0	0.0 kg/kg	Mass fraction of freshwater
ω_s	0.03 kg/kg	Mass fraction of bay water
ρ_0	1000 kg/m^3	Freshwater density
ρ_s	1020 kg/m^3	Bay water density
μ	0.001 kg/ms	Fluid viscosity

3), (4) the position (depth) and thickness of the DSW measured in points A5–A7 (see location in Figure 3), and (5) the groundwater head evolution in the inland, middle, and beach wells. The calibrated parameters were the freshwater hydraulic gradient, the hydraulic diffusivity ($D = Kb/S_y$), and the dispersivities of the system. These superparameters allowed us to estimate a combination of the values for K and S_y of the different zones that provides an accurate representation of the system (Table 1 and Figure 4). That model satisfactorily reproduces both the groundwater heads measured in the wells and the salinity in the ISC (Figures 7a–c). In the case of groundwater heads, both the general trend and the amplitude and time lag of the tidal oscillations are well captured, especially near the area of maximum interest (beach well). Hydraulic diffusivity is the critical parameter to fit the amplitude and time lag of the tidal oscillations in the groundwater heads [*Nielsen*, 1990; *Serfes*, 1991]. Calibration showed that the diffusivity coefficient of the unconfined layer also controls the maximum size of the ISC and its persistence as well as the amplitude of the higher frequency salinity oscillations. The combination of the head and concentration data constrains the value of the diffusivity coefficient to $D/b \approx 125$ in the beach area. A larger diffusivity coefficient was needed to reproduce the small oscillations observed in the inland well, whereas a smaller diffusivity coefficient was needed in the beach area to reproduce the tidal fluctuations at the beach wells. For this reason, two different parameter zones for the unconfined storage coefficient were defined in the model (Figure 4). A specific yield $S_y = 0.12$ was obtained for the unconfined intertidal zone (zone 2). The S_y used for zone 1 of the unconfined domain (0.04) is in the lower range of the specific yield values measured in the glacial deposits of the Cape Cod [*Guswa and LeBlanc*, 1985; *Masterson and Barlow*, 1997].

[31] Our model yields freshwater fluxes on the low end of the range of the previous estimates for Waquoit Bay. An assumed specific yield of 0.12 gives a calibrated value of the hydraulic conductivity of 15 m/d. This hydraulic conductivity value in the range of estimates from slug tests in the area [*Amarasekera*, 1996; *Cambareri and Eichner*,

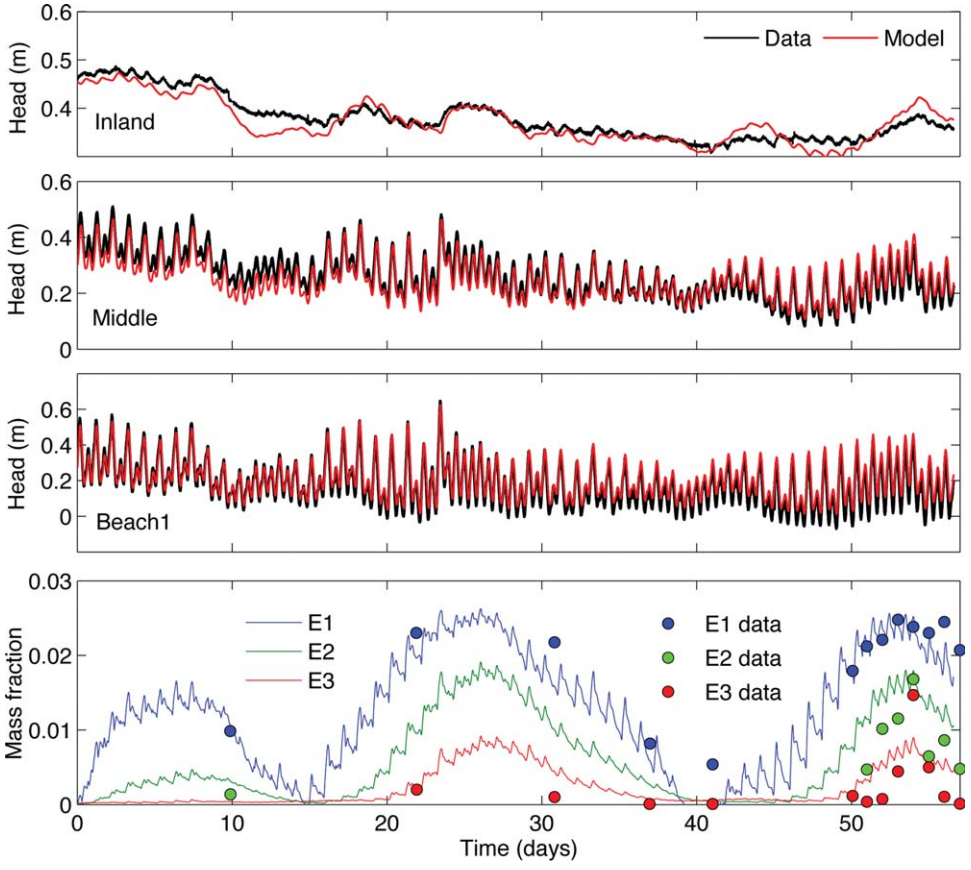

Figure 7. Simulated and measured heads in the inland, middle, and Beach1 wells and simulated and measured salinity (salt mass fraction) in sampling points E1–E3.

1998; *Michael*, 2004], but it is lower than those used in other numerical models [*Barlow and Hess*, 1993; *Michael*, 2004]. In combination with the calibrated value of the remote freshwater hydraulic gradient ($\nabla h = 0.0015$), this value of the hydraulic conductivity ($K = 15$ m/d), yields a summer freshwater flow of around 0.0225 m/d. This flux is in the range of values measured by *Michael et al*. [2003] with seepage meters but is an order of magnitude smaller than estimated by others for the same area in the literature [*Mulligan and Charette*, 2006]. Different fluxes are expected due to seasonal variability in the freshwater discharge [*Michael et al*., 2005]. *Cambareri and Eichner* [1998] estimated a freshwater flux of 0.15 m/d based on a similar estimation of the groundwater gradient ($\nabla h = 0.002$) but assuming a much higher hydraulic conductivity (73 m/d) based on *Barlow and Hess* [1993]. A much higher freshwater flow estimate (0.36 m/d) was calculated by *Mulligan and Charette* [2006] from head measurements in the wells located at the beach. However, gradients calculated from the head data in those wells are highly uncertain due to the high variability of heads induced by tides.

[32] The connection between the aquifer and the sea was represented by a leakage coefficient $\beta_0 = 1000$ d^{-1}. This value corresponds to a layer of sand 1.5 cm thick with the same value of hydraulic conductivity as the aquifer. A sensitivity analysis to these parameters (Figure S2 in the supporting information) shows that only by considerably reducing β_0 there is an effect in the calculated concentration in the intertidal zone and the modeled fluxes. That result suggests that for high values of β_0 the controlling parameter for both infiltration fluxes and the ISC extent is the aquifer permeability, whereas for very small values of β_0 this parameter becomes the key parameter.

3.4.1. Lunar Cycling of the Intertidal Cell

[33] The model reproduces the growing and waning of the ISC. At a semidiurnal scale, the ISC pulsates in response to every tide (i.e., small oscillations in simulated concentrations in Figure 7). However, the long-term ISC cycle has a duration of about 28 days. The ISC begins to grow after the neap tides of the First Quarter moon as the tidal amplitude increases. It reaches its maximum size with the high spring tides accompanying the new moon and afterward wanes as the amplitude of the tidal oscillation decreases, finally disappearing at the first quarter neap tide (Figure 8; see movie M1 in the supporting information for a detailed representation of the ISC growing cycle and the groundwater flow vectors).

[34] During the spring tides of the full moon, the ISC does not grow but wanes. To understand why the ISC only develops during the new moon we considered both the tidal signal (Figure 5) and the beach topographic profile (Figure 9a). The measured profile presents an abrupt change in slope in the beach profile (berm) above which the beach is flatter; so for a given rise in tidal elevation more beach is inundated and infiltration could be enhanced. This beach profile is termed reflective or summer and is found on beaches where berms result from onshore sediment movement.

[35] We analyzed the spatial distribution of the infiltration and the discharge to better understand the link among tides, the beach profile, and the ISC cycle. The groundwater flux at the nodes of the seaside boundary (Figure 9b) is plotted side by side with the salinity evolution at the intertidal zone (Figure 9c) during a lunar cycle to illustrate how the ISC responds to the bay water infiltration. The movement of the tidal mark, delineated by a black line in Figure 9b, indicates that the berm (Figure 9a) was inundated five times during the high tides of the new moon. The ISC growing period corresponds with the increasing high tides and with these events that flood the beach berm. Figure 9 also evidences the areas of the preferential groundwater discharge. Most of the discharge occurs in a strip of the intertidal zone located between 9 and 12 m in Figure 9b. This location coincides with the discharge strip delineated by the temperature data measured with the optic cable along the same profile during the summer of 2007 [*Henderson et al*., 2009]. This concentrated discharge includes all the freshwater discharge as well as most of the brackish discharge from the ISC and the DSW. The discharging strip moves inland and seaward during the ISC cycle (Figure 9b) following the movement of the low-tide marks. The integrated fluxes over a lunar cycle (Figure 9d) show a peak of the groundwater discharge bounded by two main infiltration areas: the inland infiltration area associated to the ISC and the seaward area of moderate seawater infiltration associated to the DSW. The infiltration declines seaward until becoming insignificant (<0.01 m^3/m) at $x = 40$ m. Note that there is no preferential infiltration at the inland part of the intertidal zone as in *Robinson et al*. [2007b] but a homogeneously distributed ISI at the central part of the intertidal zone.

[36] A close-up of the infiltration pattern during a tidal cycle (Figure 9e) reveals that infiltration occurs mainly at the tip of the advancing tide in the area just inundated, and discharge occurs on receding tides; at very low tides, water discharges above the tide mark (black line) forming a seepage face.

[37] Given the control that the beach profile has on the ISC development, changes in the beach profile may modify the cycling and presence of the ISC. Several simulations with the linear beach profiles were carried out to assess the effect of the beach profile in the development of the ISC and the distribution of the infiltration/discharge fluxes (Figure 10). Two linear profiles were simulated, one with a lower slope (F1) and one with a higher slope (F2) than the measured profile. In both cases only the upper part of the profile was modified to maintain the heads at the freshwater discharge zone. The maximum tidal mark changed accordingly, resulting in a larger infiltration area in the case of the mild slope. The results of the simulation (Figure 10c) show that the persistence of the ISC decreases in the case with high slope (shorter infiltration area). Regardless of some inflection points due to small irregularities in the topography, the flux distribution along the beach profile in the real case is a combination of the two linear profile cases (Figure 10b). The extent of the beach profile in which infiltration occurs is almost identical to the F1, although most of the infiltration occurs in the same area as in F2. The discharge distribution resembles the more constricted curve of the high-slope case (F2). This results in a large infiltration area but a rather small discharge zone. Water infiltrated in the most inland part of the beach travels at least 3 m before discharging back to the bay.

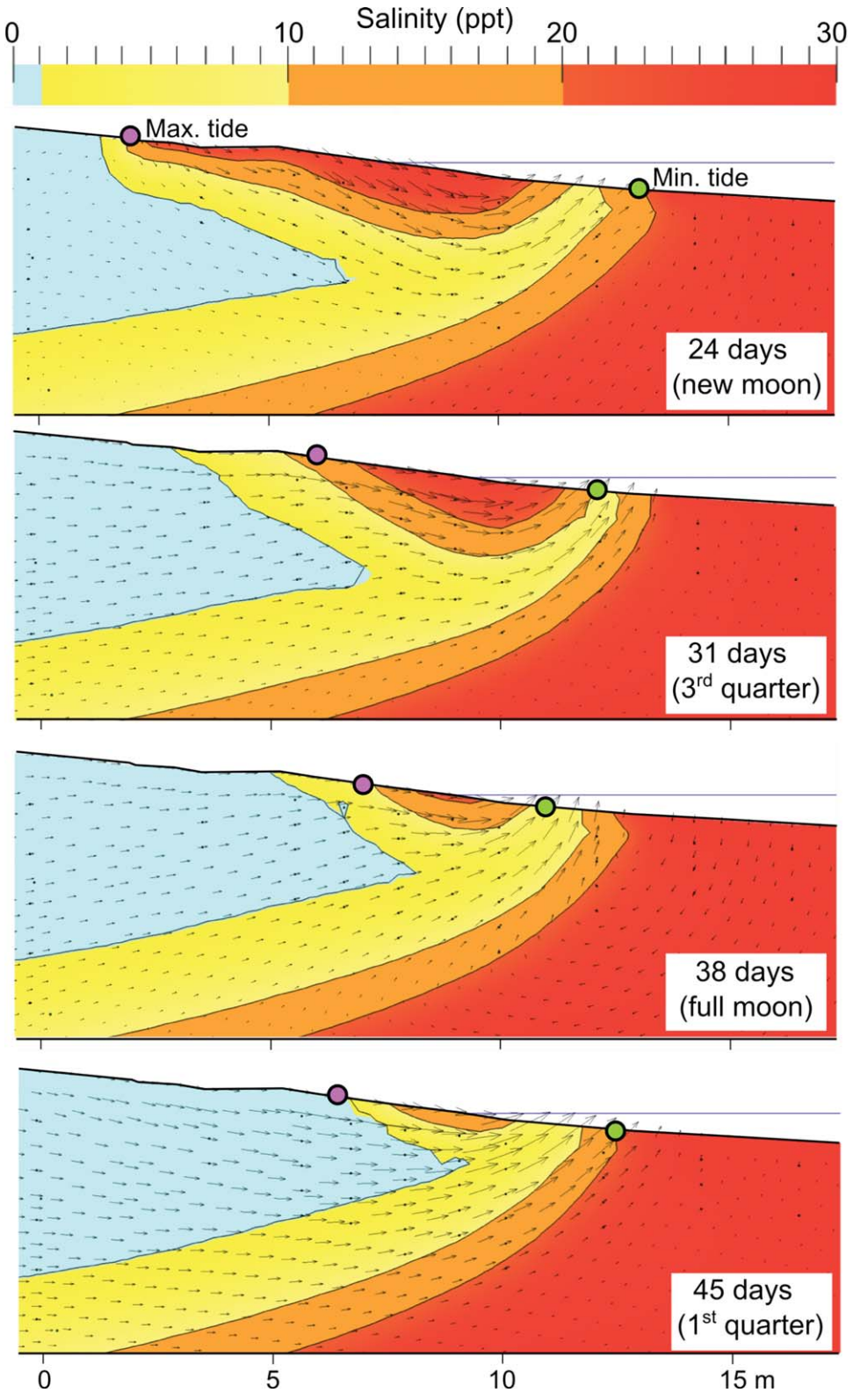

Figure 8. Simulated salinity distribution and daily phase-averaged velocity vectors at the four quarters of the lunar cycle. The ISC reaches its maximum size at the highest spring tide of new moon. Afterward, it wanes until almost disappearing by the first quarter neap tide. A complete movie of the dynamics M1 can be downloaded from the supporting information.

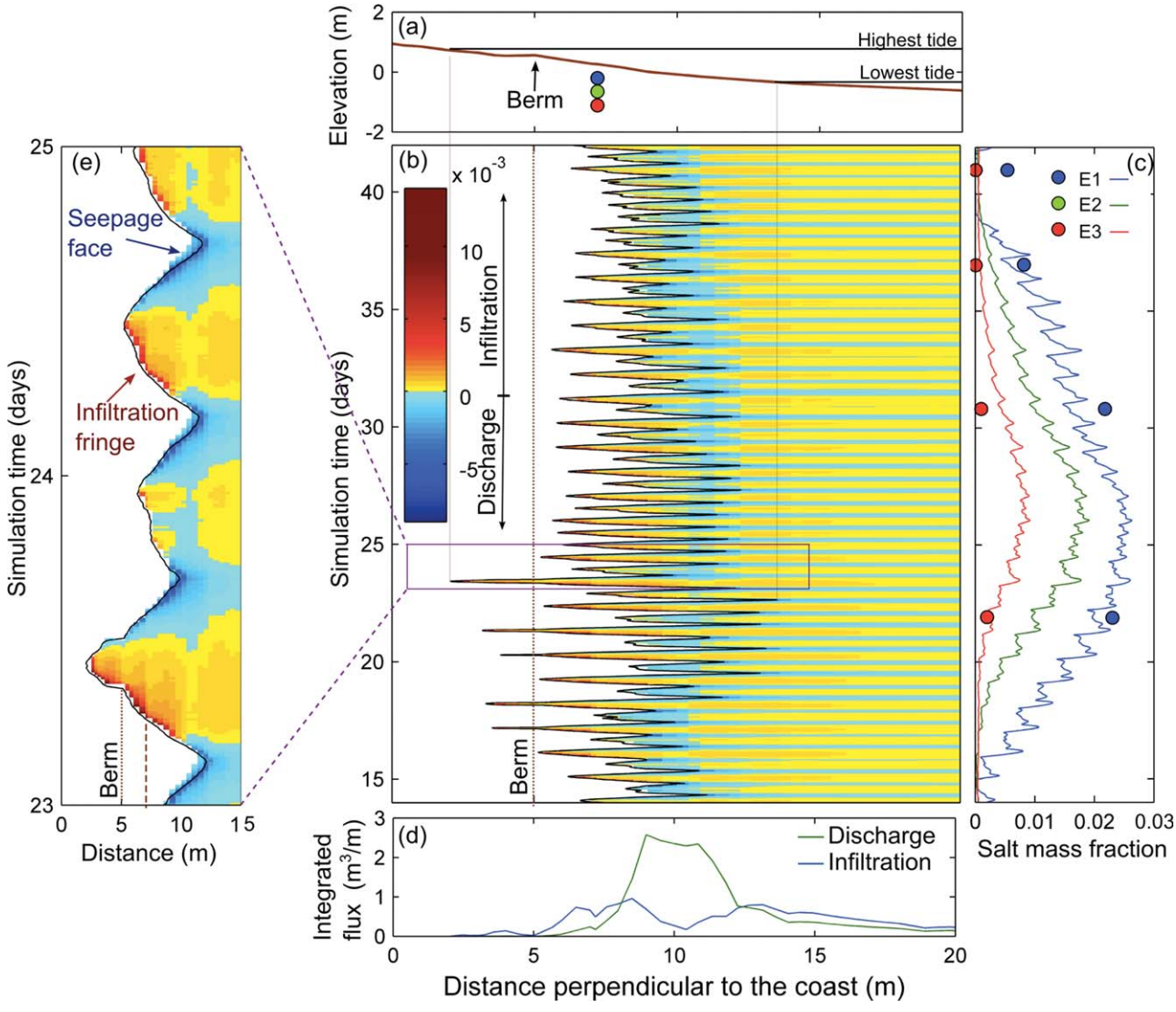

Figure 9. (a) Beach profile and location of sampling points E1–E3; (b) groundwater flux at the nodes of the seaside boundary showing the distribution of infiltration (positive values) and discharge (negative values) along the beach profile (x axis) during a lunar cycle (28 days in the y axis). The black line indicates the location of the tidal mark; (c) ISC evolution during that lunar cycle described by the measured and computed salinity at sampling points E1–E3; (d) integrated infiltration and discharge fluxes over an ISC cycle along the beach profile (m^3/m); and (e) detail of the infiltration/discharge pattern during four tidal cycles (from days 23 to 25 and from $x = 0$ to 15 m) showing a narrow infiltration fringe at the tip of the advancing tide and groundwater discharging above the tide mark at very low tides (seepage face).

3.4.2. Simulation of the Tracer Plume

[38] The calibrated model reproduces the overall movement and travel times of the tracer plume (Figure 11). The simulation (movie M2 in the supporting information) shows a slowly moving plume that rotates with tides and dilutes by mixing. The convoluted flow field created by tides results in an enhanced mixing and a slow horizontal advection. Since mixing can be an important control on chemical reactions, a proper representation of the fluctuating flow field is critical to realistically reproduce mixing of contaminants or nutrients moving along this part of the aquifer. The simulation covers the first 5 days after the injection, during which data were available. It should be noted that the data of the model were not adjusted to fit the tracer data. The tracer data were not used to estimate the transport parameters of the system (dispersivity coefficients) because we have no data to quantify tracer dispersion perpendicular to the transect. However, the tracer transport provides the qualitative understanding of flow and mixing of a solute plume moving inside the ISC.

3.4.3. Age Simulation

[39] When the ISC is fully developed, the results of the groundwater age simulation (Figure 12) show two young water areas, one within the ISC and another within the DSW that reaches deeper than the ISC. Young groundwater evidences fast groundwater recirculation within these cells. The presence of young groundwater in the intertidal zone is associated with the ISC cycle, and therefore, it disappears during the lunar cycle as the ISC disappears.

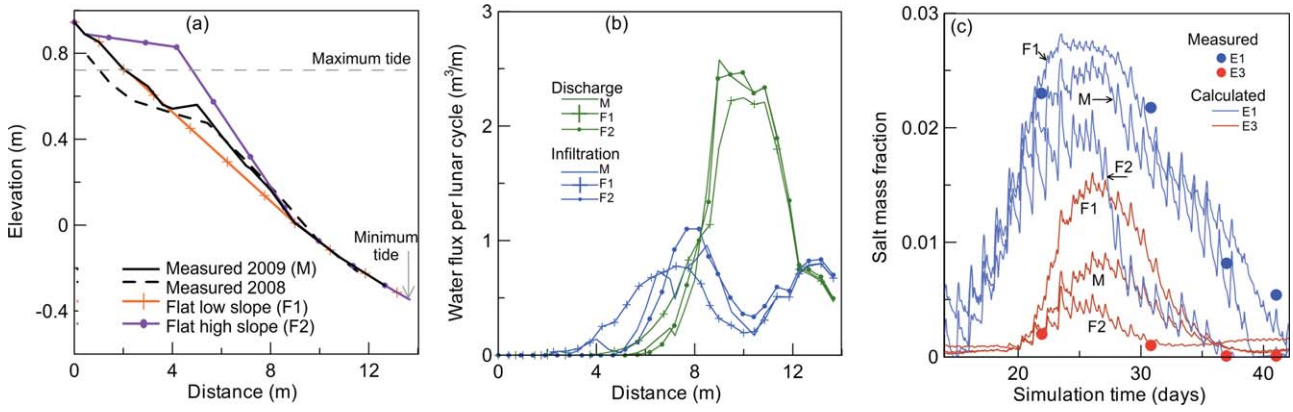

Figure 10. Sensitivity analysis to the beach morphology: (a) beach profiles, (b) recharge and discharge integrated over an ISC cycle (m^3/m), and (c) simulated concentration in points E1 and E3 showing the cycling and persistence of the ISC.

[40] At the ISC, the collocation of high salinity and young age, with parallel contours, evidences infiltration at the center of the ISC. This is consistent with the higher ISI at the central part of the intertidal zone over a lunar cycle (Figure 10d). The older ages on the fringe of the ISC are the result of mixing with old freshwater. Our result differs from the flow lines calculated using a steady-state groundwater flow simulation with phase-averaged periodic boundary conditions [*Robinson et al*., 2007b], in which water infiltrates in the inland part of the ISC and moves parallel to the salinity isolines to discharge in the lowest part of the ISC. The reason for this discrepancy is the control of both mixing and the ISC cycle (growing and decaying) in groundwater pathways. The ISC size is continuously changing preventing the development of steady-state pathways.

[41] The different residence times and dynamics in this system may control the extent of geochemical reactions, delineating different geochemical zones. The groundwater ages mapped in Figure 12 support the *Michael et al*.'s finding [2011] that radium isotopes differ among the zones. For example, Michael et al. found that the ISC has low concentrations of long-lived isotopes, even lower that bay water in some cases, whereas the brackish water where the DSW mixes with FGD has much higher concentrations of long-lived isotopes. Thus, it appears that young groundwater

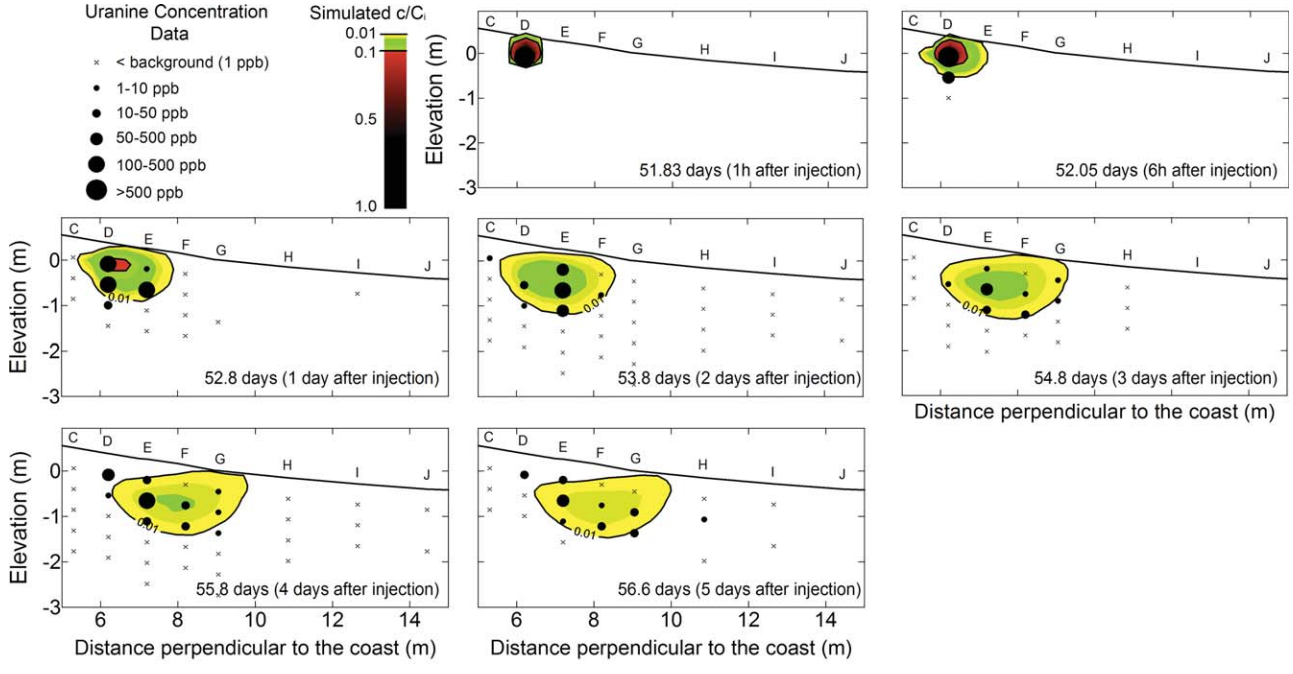

Figure 11. Simulated tracer plume and tracer data obtained during the first 5 days after injection. The simulated concentration has been normalized by the initial concentration at the injection point. The isolines delineate 10% and 1% of the initial concentration. A complete movie of the simulated tracer test M2 can be downloaded from the supporting information.

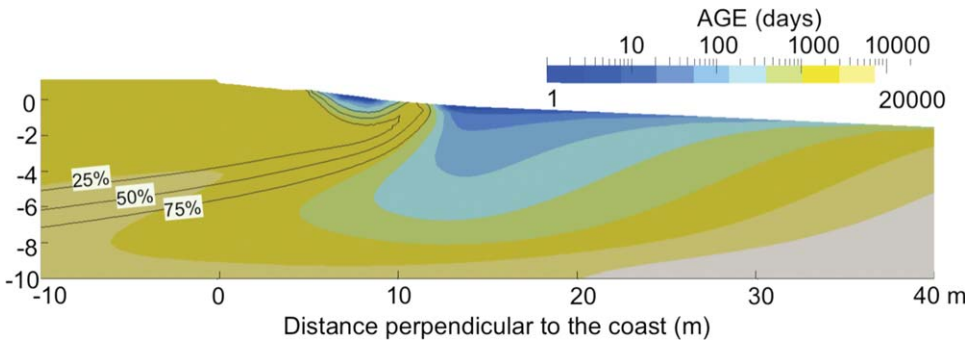

Figure 12. Groundwater age distribution around the discharge zone (color contours) and salinity isolines (25%, 50%, and 75% of saltwater) at new moon, when the ISC is fully developed. The groundwater age distribution evidences the location of the two fast saltwater recirculation cells: (1) within the ISC and (2) within the DSW. The freshwater at the discharge zone has a relative age above 5 years.

ages in the ISC inhibit the ingrowth of the long-lived radium isotopes.

[42] The results of the groundwater age simulation emphasize the control of the ISC cycle in groundwater pathways at the intertidal zone and the importance of mixing in coastal aquifers affected by tidal forcing.

3.5. Discussion: Relation of Groundwater Fluxes to Tides

[43] SGD, and hence the solute loads delivered to the coastal ocean, varies with tides. The results presented here clarify how the tidal cycle affects the groundwater inflow and discharge. SGD is defined as all the fluxes of groundwater to the ocean, independently of their forcing mechanism and chemistry. Here we consider SGD to be composed by a freshwater component, FGD, and two saltwater components, ISD and DSD, depending on the origin (Figure 1). The total saltwater infiltration (TSI) is constituted by ISI and DSI (its ISC and DSW components, respectively). We focused on the relationship of groundwater fluxes to the maximum, the minimum, and the moving average of tide elevation over a tidal day, 0050 h (Figure 13a). Hereafter, the moving average will be referred as the mean tidal elevation. The modeled fluxes were also averaged over a tidal day (Figure 13b). The relation of the fluxes over time to the tides was considered by temporal correlograms (correlations versus time lags) of the computed fluxes and the tidal attributes (Figure 14).

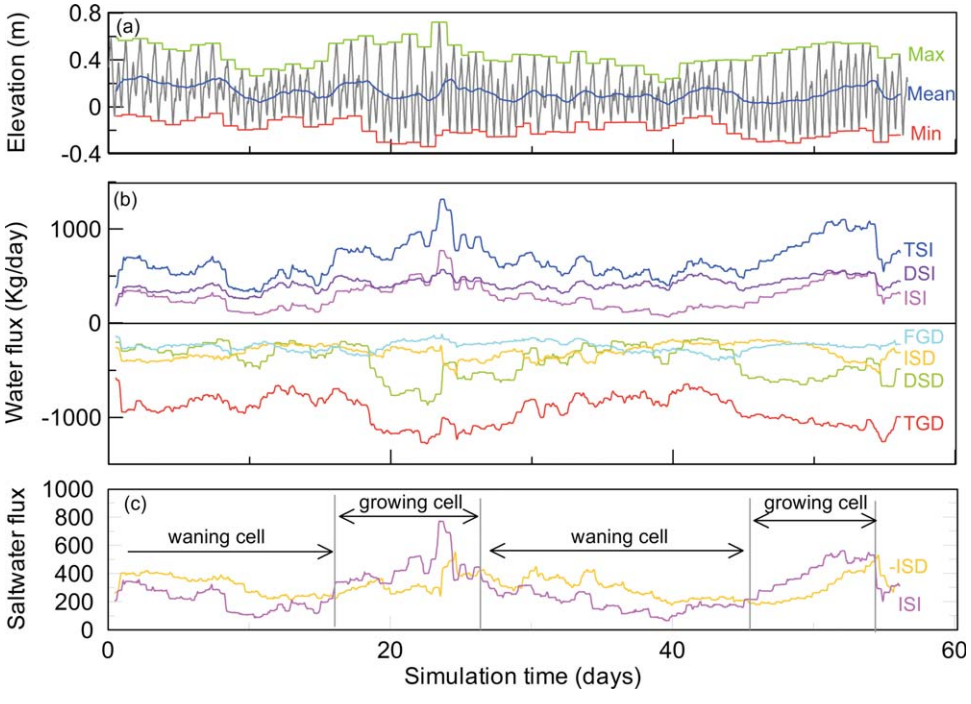

Figure 13. (a) Tide signal and averaged minimum, maximum, and mean tide compared to the total averaged fluxes across the seaside boundary and their different components; (b) temporal evolution of SGD and TSI and its individual components (averaged over a tidal day); and (c) intertidal fluxes ISI and ISD and phases of the ISC cycle.

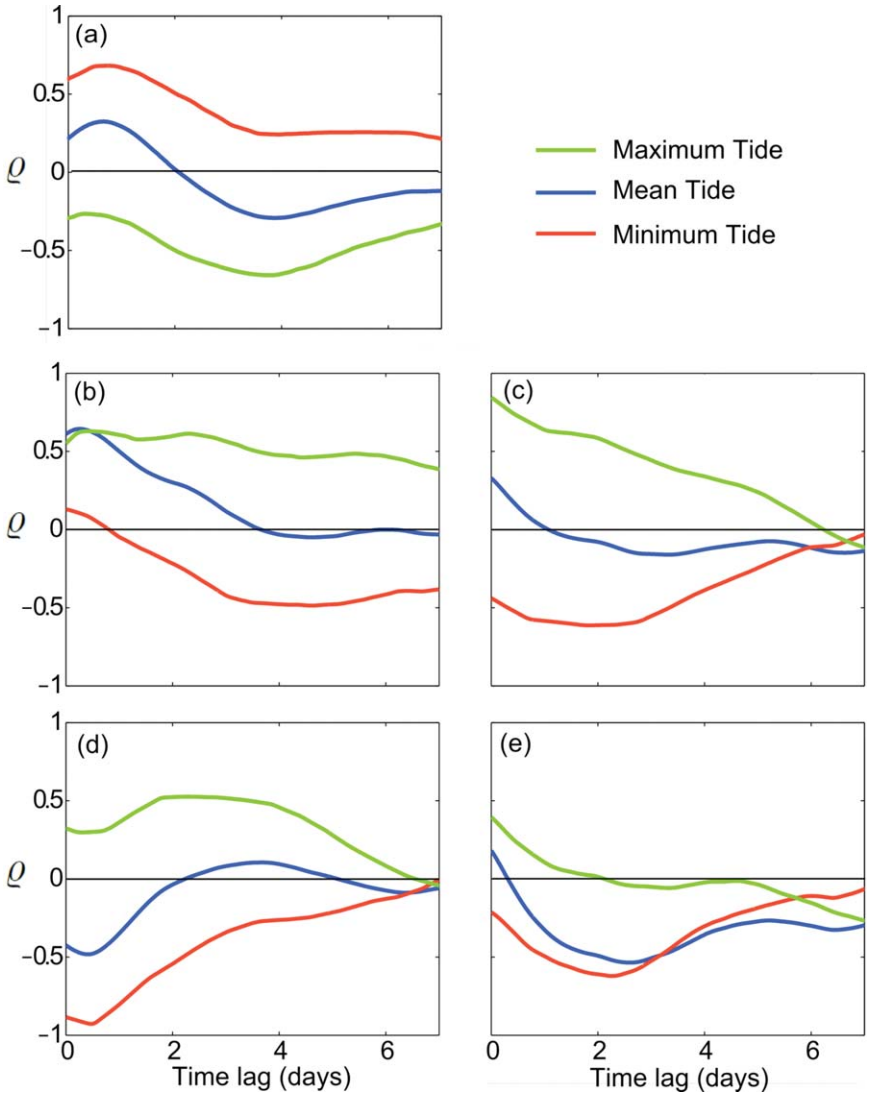

Figure 14. Correlograms of the different averaged fluxes and the parameters characterizing the tidal signal: (a) FGD, (b) ISD, (c) ISI, (d) DSD, and (e) DSI.

[44] Although the upstream inflow of freshwater, at 150 m upland from the coast, is constant, FGD (Figure 13b) varies over time due to tides so that the storage of freshwater in the aquifer increases or decreases. FGD diminishes when the ISC is present, indicating that the ISC enhances the storage of freshwater in the aquifer. FGD correlates positively with the minimum tide elevation, with a lag of 1 day (correlation coefficient, $\varrho \approx 0.7$; Figure 14a), and to a much lesser extent with the mean tide ($\varrho \approx 0.3$). This counterintuitive result that FGD increases with a higher low tide is linked to the inland movement of the saltwater-freshwater interface. When low tides are relatively high, the freshwater-DSW interface rises and moves inland, increasing FWD by displacing freshwater, but also lifting the water table. This building up continues during the rising tide. At the following low minimum tide the stored freshwater is released, temporarily increasing FGD and explaining the 1 day lag in the maximum correlation. Therefore, higher FGD is expected at the neap tides when higher low tides often occur. This result is consistent with the observations of the enhanced freshwater discharge and nutrients during the neap tides at Stinson Beach, California [*de Sieyes et al.*, 2008].

[45] Both ISI and ISD are linked to the lunar cycle, with a maximum inflow and outflow at the highest spring tides of the new moon. The ISC grows when the ISI is greater than ISD and wanes when the ISD is greater (Figure 13c). Therefore, growing starts after the neap tides preceding the new moon, as the tidal amplitude increases. After the new moon, as the tidal amplitude is reduced, the ISD is dominant, and the ISC wanes. The growing period extends for about 7 days, shorter than the discharge cycle that takes around 15 days. The ISI has a strong correlation with the maximum tide ($\varrho \approx 0.8$) that decays over several days, as there are usually several consecutive days of high tides. The ISD (Figure 14b) shows a weaker correlation ($\varrho \approx 0.5$) with the maximum tide, but this correlation extends for over 7 days, indicating how the saltwater previously accumulated in the ISC is slowly drained as the tidal amplitude decreases.

[46] DSD varies with the lunar cycle through a very strong inverse correlation ($\varrho \approx 0.95$) with the minimum tide elevation (Figure 14c). During low minimum tides, the freshwater-DSW interface moves seaward and downward, driving saline discharge. The close match between DSD and the low-tide elevation is consistent with the positive correlation between the FGD and the minimum tidal elevation: for relatively higher minimum tides, the interface moves inward and up, decreasing saline discharge, but increasing the freshwater discharge; for low minimum tides the interface drops, driving saline discharge and capturing freshwater before it discharges. The mild ($\varrho \approx 0.5$) lagged positive correlation of DSD with the maximum tide elevation can be linked to the development of the ISC. When the ISC forms, it pushes the interface seaward and downward, as shown also by the salinity data in Figure 6, driving DSD. Of all the five components of groundwater-seawater exchange, DSI varies the least with tides (Figure 13b). There are no strong correlations (>0.5) between the DSI and any of the tidal variables (Figure 14e). This result is striking given the nearly perfect correlation of DSD with the minimum tide and implies that the changes in the size of the DSW are driven more by changes in discharge than changes in seawater inflow.

4. Conclusions

[47] Tides create complex flow patterns that result in variability in the discharge fluxes and enhanced mixing between fresh and saline groundwater that can drive chemical reactions [*Rezaei et al*., 2005; *De Simoni et al*., 2005]. We present field evidence of the complex interaction among the intertidal saline cell, the DSW, and the freshwater discharge.

[48] Salinity surveys and a tracer test experiment at Waquoit Bay, Massachusetts, evidenced a growing and waning ISC with a slow recirculation of saltwater. Saltwater accumulates at very high tides because infiltration during the rising tide is larger than saltwater outflow during the receding tide. However, when the maximum tidal elevation decreases, the saltwater discharge is larger than the infiltration for a single tidal cycle, and the ISC wanes until disappear. This observation is consistent with that of *Robinson et al*. [2007c]. At their site, both the new moon and full moon spring tides were of nearly equal magnitude, so their dominant cycle lasted 14 days. At Waquoit Bay, the growing and waning cycle lasts 4 weeks since only the spring tides during the new moon are high enough to create infiltration rates that grow the ISC, and the ISC diminished more fully than in Robinson's study. The transport of solutes in the intertidal zone is strongly controlled by the ISC cycle, as it enhances mixing between the freshwater and the saltwater and controls the flow paths and the residence times.

[49] Our results are consistent with the previous work showing that the total SGD varies with the lunar cycle of tides, but our results also break down the components of SGD to show how these components vary in response to the tidal changes. Tides have the monthly and daily variability in their minimum, maximum, and mean elevations. We observed that even in the case of the small tidal amplitude (lower than 0.5 m), changes in the average tide and in the maximum and minimum tides can significantly influence fluxes across the seaside boundary. The maximum tides control infiltration and discharge at the intertidal zone, whereas the minimum tide modulates the FGD and DSD, increasing one of them when decreasing the other. Thus, FGD is enhanced during higher minimum tides (e.g., neap low tides) and DSD during low minimum tides. The coupling between the transient ISC and the saltwater fluxes evidences the need to understand the dynamic behavior of the system to properly estimate the saltwater discharge fluxes and the SGD in general. Measurements that span at least one full lunar cycle appear to be necessary to characterize the coastal groundwater exchange.

References

Abarca, E., J. Carrera, X. Sanchez Vila, and M. Dentz (2007), Anisotropic dispersive Henry problem, *Adv. Water Resour.*, *30*(4), 913–926.

Amarasekera, K. (1996), *Groundwater flow and mass transport model of the Main Base Landfill site at the Massachusetts military reservation*, Ph.D. dissertation, Mass. Inst. of Technol., Cambridge, Mass.

Barlow, E., and K. Hess (1993), *Simulated hydrologic responses of the Quashnet River stream-aquifer system to proposed ground-water withdrawals, USGS Water-Resour. Invest. Rep. 93-4064*, 52.

Behrens, H., et al. (2001), Toxicological and ecotoxicological assessment of water tracers, *Hydrogeol. J.*, *9*(3), 321–325.

Bethke, C. M., and T. M. Johnson (2008), Groundwater age and groundwater age dating, *Ann. Rev. Earth Planet. Sci.*, *36*, 121–152, doi:10.1146/annurev.earth.36.031207.124210.

Bowen, J. L., K. D. Kroeger, G. Tomasky, W. J. Pabich, M. L. Cole, R. H. Carmichael, and I. Valiela (2007), A review of land-sea coupling by groundwater discharge of nitrogen to New England estuaries: Mechanisms and effects, *Appl. Geochem.*, *22*(1), 175–191.

Brovelli, A., X. Mao, and D. A. Barry (2007), Numerical modeling of tidal influence on density-dependent contaminant transport, *Water Resour. Res.*, *43*, W10426, doi:10.1029/2006WR005173.

Cambareri, T. C., and E. M. Eichner (1998), Watershed delineation and ground water discharge to a coastal embayment, *Ground Water*, *36*(4), 626–634.

Charette, M. A., and E. R. Sholkovitz (2006), Trace element cycling in a subterranean estuary: Part 2. Geochemistry of the pore water, *Geochim. Cosmochim. Acta*, *70*(4), 811–826, doi:10.1016/j.gca.2005.10.019.

Cooper, H.H. (1964), *A hypothesis concerning the dynamic balance of fresh water and salt water in a coastal aquifer, USGS Water-Supply Pap. 1613-C*.

de Sieyes, N. R., K. M. Yamahara, B. A. Layton, E. H. Joyce, and A. B. Boehm (2008), Submarine discharge of nutrient-enriched fresh groundwater at Stinson Beach, California is enhanced during neap tides, *Limnol. Oceanogr.*, *53*(4), 1434–1445.

De Simoni, M., J. Carrera, X. Sanchez Vila, and A. Guadagnini (2005), A procedure for the solution of multi-component reactive transport problems, *Water Resour. Res.*, *41*, W11410, doi:10.1029/2005WR004056.

Destouni, G., and C. Prieto (2003), On the possibility for generic modeling of submarine groundwater discharge, *Biogeochemistry*, *66*(1–2), 171–186.

Faunt, C. C., A. M. Provost, M. C. Hill, and W. R. Belcher (2011), Comment on "An unconfined groundwater model of the Death Valley Regional Flow System and a comparison to its confined predecessor" by RWH Carroll, GM Pohll and RL Hershey [J. of Hydrol. 373/3–4, pp. 316–328], *J. Hydrol.*, *397*(3–4), 306–309, doi:10.1016/j.jhydrol.2010.11.038.

Flury, M., and N. N. Wai (2003), Dyes as tracers for vadose zone hydrology, *Rev. Geophys.*, *41*(1), 1002, doi:10.1029/2001RG000109.

Gardner, L. R., and A. M. Wilson (2006), Comparison of four numerical models for simulating seepage from salt marsh sediments, *Estuar. Coast. Shelf Sci.*, *69*(3–4), 427–437, doi:10.1016/j.ecss.2006.05.009.

Gingerich, S., and C. I. Voss (2005), Three-dimensional variable-density flow simulation of a coastal aquifer in southern Oahu, Hawaii, USA, *Hydrogeol. J.*, *13*(2), 436–450, doi:10.1007/s10040-004-0371-z.

Goode, D. J. (1996), Direct simulation of groundwater age, *Water Resour. Res.*, *32*(2), 289–296.

Guswa, J. H., and D. R. LeBlanc (1985), *Digital flow models of groundwater flow in the Cape Cod aquifer system, Massachusetts, USGS Water-Supply Pap. 2209*, 112.

Henderson, R. D., F. D. Day Lewis, and C. F. Harvey (2009), Investigation of aquifer-estuary interaction using wavelet analysis of fiber-optic temperature data, *Geophys. Res. Lett.*, *36*, L06403, doi:10.1029/2008GL036926.

Henderson, R. D., F. D. Day Lewis, E. Abarca, C. F. Harvey, H. N. Karam, L. B. Liu, and J. W. Lane (2010), Marine electrical resistivity imaging of submarine groundwater discharge: Sensitivity analysis and application in Waquoit Bay, Massachusetts, USA, *Hydrogeol. J.*, *18*(1), 173–185, doi:10.1007/s10040-009-0498-z.

Hidalgo, J. J., L. J. Slooten, A. Medina, and J. Carrera (2005), *A Newton-Raphson based code for seawater intrusion modelling and parameter estimation, in Groundwater and Saline Intrusion: Selected Papers From the 18th Salt Water Intrusion Meeting*, edited by L. Arguás, E. Custodio, and M. Manzano, pp. 111–120, IGME, Madrid.

Janik, D. (1987), *State of the aquifer report, Tech. Rep., Cape Cod Plann. and Econ*. Dev. Comm., Barnstable, Mass.

Kasnavia, T., D. Vu, and D. A. Sabatini (1999), Fluorescent dye and media properties affecting sorption and tracer selection, *Ground Water*, *37*(3), 376–381, doi:10.1111/j.1745-6584.1999.tb01114.x.

Kohout, F. (1964), *The flow of fresh water and salt water in the Biscayne Bay Aquifer of the Miami area, Florida, in Seawater in Coastal Aquifers, Water Supply Pap. 161G-C*, pp. 12–32, U.S. Geol. Surv., Washington, D. C.

Lebbe, L. (1999), Parameter identification in fresh-saltwater flow based on borehole resistivities and freshwater head data, *Adv. Water Resour.*, *22*(8), 791–806.

LeBlanc, D., J. Guswa, M. Frimpter, and C. Londquist (1986), *Groundwater resources of Cape Cod, Massachusetts, Hydrol. Invest. Atlas 692, 4 plates*, U.S. Geol. Surv., Reston, Va.

Li, L., D. A. Barry, F. Stagnitti, and J. Y. Parlange (1999), Submarine groundwater discharge and associated chemical input to a coastal sea, *Water Resour. Res.*, *35*(11), 3253–3259.

Magal, E., N. Weisbrod, A. Yakirevich, and Y. Yechieli (2008), The use of fluorescent dyes as tracers in highly saline groundwater, *J. Hydrol.*, *358*(1–2), 124–133, doi:10.1016/j.jhydrol.2008.05.035.

Maji, R., and L. Smith (2009), Quantitative analysis of seabed mixing and intertidal zone discharge in coastal aquifers, *Water Resour. Res.*, *45*, W11401, doi:10.1029/2008WR007532.

Masterson, J. P., and P. M. Barlow (1997), Effects of simulated groundwater pumping and recharge on ground-water flow in Cape Cod, Martha's Vineyard, and Nantucket Island Basins, Massachusetts, USGS Water Supply Pap. 2447.

Michael, H. A. (2004), *Seasonal dynamics in coastal aquifers: Investigation of submarine groundwater discharge through field measurements and numerical models*, Ph.D. dissertation, Mass. Inst. of Technol., Cambridge, Mass.

Michael, H. A., J. S. Lubetsky, and C. F. Harvey (2003), Characterizing submarine groundwater discharge: A seepage meter study in Waquoit Bay, Massachusetts, *Geophys. Res. Lett.*, *30*(6), 1297, doi:10.1029/2002GL016000.

Michael, H. A., A. E. Mulligan, and C. F. Harvey (2005), Seasonal oscillations in water exchange between aquifers and the coastal ocean, *Nature*, *436*(7054), 1145–1148.

Michael, H. A., M. A. Charette, and C. F. Harvey (2011), Patterns and variability of groundwater flow and radium activity at the coast: A case study from Waquoit Bay, Massachusetts, *Mar. Chem.*, *127*, 100–114, doi:10.1016/j.marchem.2011.08.001.

Mulligan, A. E., and M. A. Charette (2006), Intercomparison of submarine groundwater discharge estimates from a sandy unconfined aquifer, *J. Hydrol.*, *327*(3–4), 411–425, doi:10.1016/j.jhydrol.2005.11.056.

Neuman, S. P. (1974), Effect of partial penetration on flow in unconfined aquifers considering delayed gravity response, *Water Resour. Res.*, *10*(2), 303–312, doi:10.1029/WR010i002p00303.

Nielsen, P. (1990), Tidal dynamics of the water-table in beaches, *Water Resour. Res.*, *26*(9), 2127–2134, doi:10.1029/WR026i009p02127.

Oldale, R. N., and W. P. Dillon (1981), Episodic growth of Holocene tidal marshes in the northeastern United States—A possible indicator of eustatic sea-level fluctuations, *Geology*, *9*(9), 389–390.

Prieto, C., and G. Destouni (2005), Quantifying hydrological and tidal influences on groundwater discharges into coastal waters, *Water Resour. Res.*, *41*, W12427, doi:10.1029/2004WR003920.

Reeves, H. W., P. M. Thibodeau, R. G. Underwood, and L. R. Gardner (2000), Incorporation of total stress changes into the ground water model SUTRA, *Ground Water*, *38*(1), 89–98.

Reilly, T. E., and A. W. Harbaugh (1993), Simulation of cylindrical flow to a well using the united-states geological survey modular finite-difference groundwater-flow model, *Ground Water*, *31*(3), 489–494, doi:10.1111/j.1745-6584.1993.tb01851.x.

Rezaei, M., E. Sanz, E. Raeisi, E. Vázquez Suñé, C. Ayora, and J. Carrera (2005), Reactive transport modeling of calcite dissolution in the saltwater mixing zone, *J. Hydrol.*, *311*(1–14), 282–298.

Robinson, C., B. Gibbes, and L. Li (2006), Driving mechanisms for groundwater flow and salt transport in a subterranean estuary, *Geophys. Res. Lett.*, *33*, L03402, doi:10.1029/2005GL025247.

Robinson, C., B. Gibbes, H. Carey, and L. Li (2007a), Salt-freshwater dynamics in a subterranean estuary over a spring-neap tidal cycle, *J. Geophys. Res. Oceans*, *112*(C9), C09007, doi:10.1029/2006JC003888.

Robinson, C., L. Li, and D. A. Barry (2007b), Effect of tidal forcing on a subterranean estuary, *Adv. Water Resour.*, *30*(4), 851–865, doi:10.1016/j.advwatres.2006.07.006.

Robinson, C., L. Li, and H. Prommer (2007c), Tide-induced recirculation across the aquifer-ocean interface, *Water Resour. Res.*, *43*, W07428, doi:10.1029/2006WR005679.

Robinson, C., A. Brovelli, D. A. Barry, and L. Li (2009), Tidal influence on BTEX biodegradation in sandy coastal aquifers, *Adv. Water Resour.*, *32*(1), 16–28, doi:10.1016/j.advwatres.2008.09.008.

Serfes, M. E. (1991), Determining the mean hydraulic-gradient of groundwater affected by tidal fluctuations, *Ground Water*, *29*(4), 549–555.

Smart, P. L., and I. M. S. Laidlaw (1977), An evaluation of some fluorescent dyes for water tracing, *Water Resour. Res.*, *13*(1), 15–33, doi:10.1029/WR013i001p00015.

Smith, A. J. (2004), Mixed convection and density-dependent seawater circulation in coastal aquifers, *Water Resour. Res.*, *40*, W08309, doi:10.1029/2013WR002977.

Souza, W. R., and C. I. Voss (1987), Analysis of an anisotropic coastal system using variable-density flow and solute transport simulation, *J. Hydrol.*, *92*, 17–41.

Spiteri, C., C. P. Slomp, M. A. Charette, K. Tuncay, and C. Meile (2008), Flow and nutrient dynamics in a subterranean estuary (Waquoit Bay, MA, USA): Field data and reactive transport modeling, *Geochim. Cosmochim. Acta*, *72*(14), 3398–3412, doi:10.1016/j.gca.2008.04.027.

UNESCO (1983), Algorithms for computation of fundamental properties of seawater, *UNESCO Tech. Pap. in Mar. Sci. 44*.

Urish, D. W., and T. E. McKenna (2004), Tidal effects on ground water discharge through a sandy marine beach, *Ground Water*, *42*(7), 971–982, doi:10.1111/j.1745-6584.2004.tb02636.x.

Valiela, I., J. Costa, K. Foreman, J. M. Teal, B. Howes, and D. Aubrey (1990), Transport of groundwater-borne nutrients from watersheds and their effects on coastal waters, *Biogeochemistry*, *10*(3), 177–197.

Valiela, I., et al. (1992), Couplings of watersheds and coastal waters—Sources and consequences of nutrient enrichment Waquoit Bay, Massachusetts, *Estuaries*, *15*(4), 443–457.

Vandenbohede, A., and L. Lebbe (2006), Occurrence of salt water above fresh water in dynamic equilibrium in a coastal groundwater flow system near De Panne, Belgium, *Hydrogeol. J.*, *14*(4), 462–472, doi:10.1007/s10040-005-0446-5.

Varni, M., and J. Carrera (1998), Simulation of groundwater age distributions, *Water Resour. Res.*, *34*(12), 3271–3281.

Wang, H. (2000), *Theory of Linear Poroelasticity With Applications to Geomechanics and Hydrogeology*, Princeton Univ. Press, Princeton, N. J.

Westbrook, S. J., J. L. Rayner, G. B. Davis, T. P. Clement, P. L. Bjerg, and S. T. Fisher (2005), Interaction between shallow groundwater, saline surface water and contaminant discharge at a seasonally and tidally forced estuarine boundary, *J. Hydrol.*, *302*(1–4), 255–269.

Wilson, A. M., and L. R. Gardner (2006), Tidally driven groundwater flow and solute exchange in a marsh: Numerical simulations, *Water Resour. Res.*, *42*, W01405, doi:10.1029/2005WR004302.